ELSEVIER

International Journal of Heat and Fluid Flow 21 (2000) 640–647

International Journal of
HEAT AND
FLUID FLOW

www.elsevier.com/locate/ijhff

# Large eddy simulation of the influence of high free-stream turbulence on a spatially evolving boundary layer

Frédéric Péneau [a,*], Henri Claude Boisson [b], Ned Djilali [c]

[a] Ceram EAI Tech, 157 rue Albert Einstein, BP 085, 06902 Sophia Antipolis Cedex, France
[b] Institut de Mécanique des Fluides de Toulouse, av. Pr Camille Soula, 31400 Toulouse, France
[c] Department of Mechanical Engineering, University of Victoria, Victoria, BC, Canada V8W 3P6

**Abstract**

The influence of a high free-stream turbulent field on a spatially evolving turbulent flat plate boundary layer is investigated using large eddy simulation (LES) with a dynamic mixed subgrid-scale model. The evolutions of skin friction, heat transfer coefficient, and flow and thermal field are presented and analyzed. The impact of free-stream turbulence on shear stress and velocity profiles is minimal, whereas substantial heat transfer augmentation is predicted together with a modification of the temperature profiles in the logarithmic and wake regions. © 2000 Begell House Inc. Published by Elsevier Science Inc. All rights reserved.

## 1. Introduction

Our understanding of the turbulent mechanisms and interactions between the large-scale structures in a turbulent boundary layer and the small dissipative structures is limited. The influence of a very high free-stream turbulence on these interactions is even less well understood, despite numerous experimental studies undertaken over the last 20 year (Maciejewski and Moffat, 1992; Blair, 1983; Hancock and Bradshaw, 1989).

This type of flow is indeed one of the most important industrial heat transfer problems. Recent studies have shown that the thermal field is more sensitive to the free-stream turbulence than the dynamic field (Maciejewski and Moffat, 1992). This difference in behavior underscores a relationship between the temperature and velocity field that is more complex than implied by the passive scalar approach.

In this paper, spatial large eddy simulations of this flow are undertaken to elucidate some of these issues. The improved version of Zang et al. (1993) of the "dynamic subgrid-scale eddy viscosity model" (Germano et al., 1991) was used in the present simulations. This dynamic mixed model (DMM) computes locally the subgrid viscosity and diffusivity allowing the model to not only capture the energy backscatter of the small eddies towards the large ones, but also to exhibit the correct asymptotic behavior in the vicinity of solid walls without having to resort to a damping function. This latter feature of the model allows us to undertake the study of the influence of a high free-stream turbulent on the dynamic and heat transfer coefficients, since these are not imposed via an assumed law.

Many of the direct and large eddy simulations (LES) of turbulent flows performed to date are temporal simulations (channel flow, mixing layer). For the problem of interest here, one cannot perform a temporal simulation, since there is no periodicity in the streamwise direction. Consequently, we undertook a spatial simulation of a flat plate turbulent boundary layer, and had therefore to deal with the problem of open exit and entrance boundary conditions. Whereas open boundary conditions are well documented in the literature, very little information is available on the prescription of entrance conditions appropriate for this type of problem. Strictly, it is necessary to prescribe a velocity field with the correct turbulent energy spectrum as well as the correct spatial coherence. An inlet condition based on linear stochastic estimation (LSE) of velocity time histories has been implemented for this study. This approach allows us to obtain a fully turbulent flat plate boundary layer from the beginning of the domain. The longitudinal domain length required is thereby substantially reduced and the major part of the calculation box is devoted to the analysis of the problem rather than to the development of the flow. This new entrance condition, which are used for the present simulations, will not be presented in this paper, but readers are referred to Péneau et al. (1999) and Péneau (1999) for a detailed presentation.

After a brief description of the numerical method and of the dynamic mixed model (DMM) in Section 2, we present the method adopted for obtaining the free-stream turbulent fields and discuss the physical features and characteristics of these fields. In Section 4, we present the results for the high free-stream turbulence cases, and analyze the structure of the thermal and dynamic turbulent boundary layer. A detailed examination of the flow is also undertaken near the leading edge of the flat plate when it is first "attacked" by the high free-stream turbulent field.

---

[*] Corresponding author. Tel.: +33-493-95-44-97; fax: +33-493-95-44-06.

*E-mail address:* frederic.peneau@cote-azur.cci.fr (F. Péneau).

0142-727X/00/$ - see front matter © 2000 Begell House Inc. Published by Elsevier Science Inc. All rights reserved.
PII: S0142-727X(00)00055-2

## 2. Numerical method and subgrid modeling

### 2.1. The LES equations and the subgrid-scale model

The governing equations for LES result from a spatial filtering of the Navier–Stokes equations. Since we use a finite volume method, the filter is imposed by the discretization and corresponds to the box-filter $\bar{G}(x'_i - x_i) = 1$ if $|x'_i - x_i| \leqslant \overline{\Delta}_i$ and 0 otherwise, where $\bar{\Delta}_i$ is the local mesh spacing in the $x_i$ directions. This implicit filtering is one of the attractive features of the model since no averaging of the resolved field is required. Decomposing the velocity field into a resolved part $\overline{V}_i$ (directly computed by the code) and a subgrid part $V'_i$ (the unknown in the equations), i.e., $V_i(\vec{x},t) = \overline{V}_i(\vec{x},t) + V'_i(\vec{x},t)$. We obtain the following system of equations:

$$\begin{aligned}
&\frac{\partial \overline{V}_i}{\partial x_i} = 0,\\
&\frac{\partial \overline{V}_i}{\partial t} + \frac{\partial \overline{V}_i \overline{V}_j}{\partial x_j} = -\frac{\partial \bar{p}}{\partial x_i} + \frac{\partial [2(v + v_{\mathrm{t}})\overline{S}_{ij} - L_{ij}]}{\partial x_j},\\
&\frac{\partial \overline{T}}{\partial t} + \frac{\partial \overline{T}\,\overline{V}_j}{\partial x_j} = \frac{\partial \left[(D + D_T)\partial \overline{T}/\partial x_j - Lc_j\right]}{\partial x_j},
\end{aligned} \tag{1}$$

where $\overline{S}_{ij}$ is the strain tensor and:

$$\text{(a)}\quad L_{ij} = \overline{\overline{V}_i \overline{V}_j} - \overline{\overline{V}}_i \overline{\overline{V}}_j, \qquad \text{(b)}\quad Lc_j = \overline{\overline{T}\,\overline{V}_j} - \overline{\overline{T}\overline{V}}_j, \tag{2}$$

$$C_{ij} = \overline{\overline{V}_i V'_j} + \overline{\overline{V}_j V'_i} - \left(\overline{\overline{V}}_i \overline{V'_j} + \overline{\overline{V}}_j \overline{V'_i}\right), \tag{3}$$

$$Cc_j = \overline{\overline{T} V'_j} + \overline{\overline{V}_j T'} - \left(\overline{\overline{T}}\,\overline{V'_j} + \overline{\overline{V}}_j \overline{T'}\right), \tag{4}$$

$$\text{(a)}\quad R_{ij} = \overline{V'_i V'_j} - \overline{V'_i}\,\overline{V'_j}, \qquad \text{(b)}\quad Rc_j = \overline{T' V'_j} - \overline{T'}\,\overline{V'_j}, \tag{5}$$

$$\bar{p} = \overline{P} + (C_{kk} + R_{kk})/3, \tag{6}$$

$L_{ij}$, $Lc_j$ are calculated explicitly. The cross-terms $C_{ij}$, $Cc_j$ and $R_{ij}$, $Rc_j$, on the other hand, cannot be computed directly since $V'_i(\vec{x},t)$ is unknown. Accordingly, these terms are modeled using the classical concepts of subgrid viscosity and diffusivity (Smagorinsky, 1963) in conjunction with the DMM of Zang et al. (1993). $C_{kk}$ and $R_{kk}$ are incorporated into the pressure terms because the incompressibility condition makes the evaluation of $(C_{kk} + R_{kk})$ impossible. The subgrid viscosity $v_{\mathrm{t}} = f(\vec{x},t)$ and diffusivity $D_T = f(\vec{x},t)$ are calculated every time step at each computational volume of the domain. For further details on the DMM and the calculation procedure for evaluating the subgrid viscosity and diffusivity, the reader is referred to Péneau et al. (1999).

### 2.2. The numerical method

The numerical simulations are carried out using the JADIM code. The two-dimensional version of this code is described in Magnaudet et al. (1995) and three-dimensional version in Calmet and Magnaudet (1996); we only present here a summary of the numerical method. The momentum and scalar equations are discretized using a finite volume method with a second-order centered scheme on a staggered grid. The solution is advanced in time using a three-step Runge–Kutta (RK) procedure. The nonlinear terms of each equations are computed explicity while the diffusive terms are calculated using the semi-implicit Crank–Nicholson (CN) algorithm. This latter feature is particularly important for resolving the near-wall region without prohibitively small time steps to maintain numerical stability. To satisfy the incompressibility condition, a Poisson equation is solved by combining a direct inversion in the $(x_1, x_2)$ plane with a spectral Fourier method, in $x_3$ direction. The original version of JADIM uses a multigrid method for the third direction. This method which works well in many flows, seems to fail in the case of spatially evolving turbulent flows. The use of a spectral Fourier method, which relies on periodicity in the spanwise direction, not only increases accuracy but also results in significantly faster computations.

### 2.3. Grid and physical parameters

Due to the problem of open boundary conditions set at $\partial^2 u_i/\partial x^2 = 0$ for our simulations, the dimensions of the domain are relatively large: $L_x = 85\delta_1,\ L_y = 50\delta_1,\ L_z = 20\delta_1$, where $\delta_1$ is the displacement thickness at the entrance of the domain. The number of points in each direction are: $N_x = 96$, $N_y = 96$ and $N_z = 64$. In wall units, the mesh size in the longitudinal and spanwise directions are: $(\Delta x^+, \Delta z^+) = (38, 24)$. Near the wall, the mesh is refined in the normal direction, with the first point located at $y^+ = 0.18$. The Reynolds number at the entrance, based on $\delta_1$ is $Re_{\delta_1} = 1620$. The boundary layer thickness at the entrance of the domain is $\delta = 0.16$ m and around 0.18 m at the exit. We simulate an air flow, therefore $\Pr \simeq 0.72$. The mean free-stream velocity is $U = 1.23$ m/s, while the temperature of the free- stream flow is set at $T = 293$ K. The wall temperature is $T = 294$ K. These parameter correspond to the turbulent boundary layer under low free-stream turbulence conditions.

## 3. The high free-stream turbulence field

### 3.1. Generation of inflow boundary condition

To generate a high free-stream turbulence velocity field, we start from an initial field composed of Oseen vortices of random radii $R$ and circulation $\Gamma$. For a spanwise vortex for example, the velocity field is expressed by:

$$u = \Gamma \exp\left[\frac{-([x - x_0]^2 + [y - y_0]^2)}{2R^2}\right]\frac{[y - y_0]}{R^2}, \tag{7}$$

$$v = -\int \frac{\partial u}{\partial x}\,\mathrm{d}y \quad \text{and} \quad w = 0\ \text{m/s}, \tag{8}$$

where $x$ and $y$ are the coordinates along and normal to the plate. The same kind of expression is used for the longitudinal vortices. The radius $R$ is chosen not to exceed $\delta/2$, [1] where $\delta$ is the thickness of the turbulent boundary layer [2] under the free-stream turbulence field. The lower bound for $R$ is set at twice the local mesh size, which ensures that at least four cells define a vortex in a given plane. The circulation is chosen in the range $(\Gamma/R) \in [-b; b]$, where the value of $b$ depends on the desired turbulent intensity. Only longitudinal $\omega_x$ and spanwise $\omega_z$ vortices are generated. This does not imply that at the end the turbulent field has no transversal vortices. These vortices are generated on a domain similar to the one used for the simulation of the boundary layer. It is composed of the last 55 cells in the direction normal to the flat plate of the domain presented in Section 2.3, and of 64 and 96 cells in the transverse and longitudinal directions, respectively. The dimension of

---

[1] This does not necessarily imply that at the end the free stream turbulent field has no structures larger than $\delta$, because of possible pairing and merging.

[2] For our problem $\delta \simeq 0.17$ m ($\delta = 0.16$ m at the entrance and $\delta = 0.18$ m at the exit).

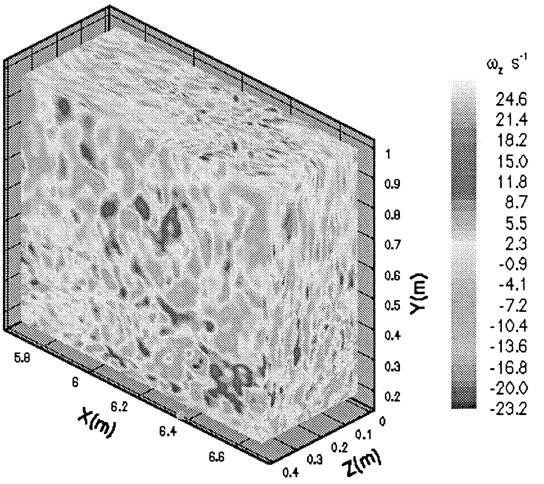

Fig. 1. Typical high free-stream turbulent field.

these cells are the same as the domain presented in Section 2.3, namely $(\Delta x^+, \Delta z^+) = (38, 24)$ the only difference being that in the longitudinal direction, no expansion of the cells is imposed at the end of the domain. This domain has then the dimensions $L_x = 50\delta_1$, $L_y = 41\delta_1$, $L_z = 20\delta_1$, where $\delta_1$ is the displacement thickness at the entrance of the domain of the boundary layer developing below the free-stream turbulent field.

Once the initial velocity field has been obtained, we start the calculation with periodic condition in the longitudinal [3] and spanwise directions and constant velocity at the upper and lower limit of our domain. These latter boundary conditions correspond to the flat plate turbulent boundary layer condition at $(y = \delta)$, where $u = 1.23$ m/s, [4] $v = w = 0$ m/s. A typical velocity field obtained after a sufficient number of time steps is illustrated in Fig. 1.

The entrance section of the spatial simulation is then decomposed in two domains in direction $y$. Domain I extends from the wall to the 41th plane $(x, z)$. Domain II contains the 55 planes up to the top of the computational domain described in Section 2.3. To introduce the turbulent field, for performing the spatial simulation of the interaction with the flat plate boundary layer, in domain II, we record $(y, z)$ plane time histories of this free-stream turbulence field. In the inner part (domain I) we use LSE (Péneau, 1999) to construct time-dependent entrance conditions. At the entrance, the height of the domain I is greater than the boundary layer thickness. This has been imposed for numerical stability purpose. The consequence of this is that the interaction between the free-stream field and the boundary layer does not take place till the entrance.

### 3.2. Characteristics

In Fig. 2, we present typical turbulent intensities profiles, where $Tu = u_{\mathrm{rms}}/U$ and $Iu = \sqrt{u'^2 + v'^2 + w'^2}/\|\vec{U}\|$, where $U$ is the local mean velocity value for $0.17 \leqslant y \leqslant 1$ m which corresponds to the ordinates of the first and last cells of the domain II. The evolution of $Iu$ is consistent with the boundary condition imposed on the free-stream turbulence, i.e., constant velocity along the top and bottom of the domain. This implies that the fluctuations of the normal velocity $v$ vanish when approaching these boundaries. As we move away from the constant velocity boundaries, the $v_{\mathrm{rms}}$ increase, reaching a maximum near the middle of the domain, hence the shape of the $Iu$ profile results. The mean $U$ velocity profile for the free-stream turbulence field was fixed to a constant mean value of 1.23 m/s within ±3% over a distance of $\delta$ above the boundary layer. This was motivated by the high sensitivity of the turbulent boundary layer to the mean pressure gradient imposed by the free-stream turbulent field observed in earlier simulations. Indeed, the first simulations undertaken with a free-stream turbulent field with a mean velocity at the interface 10% below the external mean velocity $U_e$ exhibited a distinct reduction of the skin friction coefficient. This was observed experimentally by Baskaran et al. (1989). Examination of the longitudinal and transverse spectra shows that the turbulence field is neither homogeneous nor isotropic.

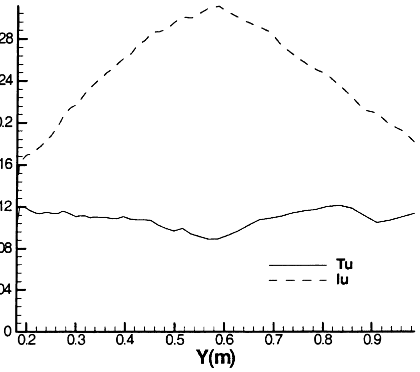

Fig. 2. Typical turbulent intensities profiles.

This conclusion is confirmed by the turbulent intensity profiles. To the question of how realistic such a turbulent field is, we note that the time evolution of the field statistics shows a decrease of the turbulent intensities as in grid turbulence. An expression of the form $K(t - t_0)^{-n}$ with $n \simeq 1$ provides a good fit for these time evolutions (see Fig. 3).

The major difference between the experimental conditions and the present simulations, is that the turbulent flat plate boundary layer has not developed under the free-stream turbulent field. This results in the $u_{\mathrm{rms}}$ profile evolution shown in Fig. 4. For our simulations, the turbulent flat plate boundary layer "senses" the presence of the turbulent field progressively. Three simulations are presented in Fig. 4. They correspond to different levels of external turbulent intensities that will be

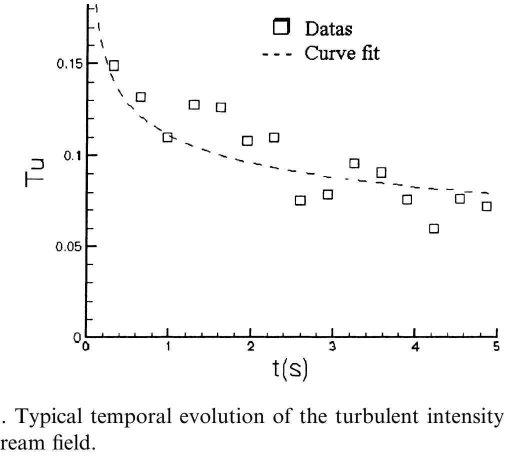

Fig. 3. Typical temporal evolution of the turbulent intensity $Tu$ of a free-stream field.

---

[3] This is the reason for the absence of cell expansion in this direction.

[4] This study is undertaken in collaboration with INRA for heat transfer in a refrigeration chamber. Typical velocities are of the order of 1 m/s.

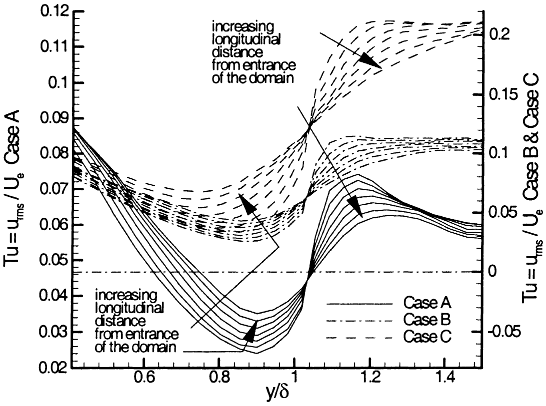

Fig. 4. Evolution of typical longitudinal $u_{\mathrm{rms}}$ profiles.

discussed in the next section. From this figure, it is difficult to establish which value is significant in driving the transfer of the turbulent boundary layer. A strong decrease in the streamwise direction of $u_{\mathrm{rms}}$ is observed just above the boundary layer, while at about $[0.8\delta; \delta]$ the opposite happens. It appears that there is no unique way of characterizing the interaction mechanism. Moreover, it might be expected that the dissipation length-scale seen by the boundary layer increases with streamwise distance. The evolution of the dissipation length-scale of the free-stream turbulent field,

$$Le_u = -\overline{u'^2}^{3/2}/(U\mathrm{d}\overline{u'^2}/\mathrm{d}x),$$

is presented in Fig. 5 for some of the cases treated, where $\beta = Tu/(Le_u/\delta_{995} + 2)$ is a parameter used and defined by Hancock and Bradshaw (1983, 1989). In this figure, the range of length-scales is large. Nevertheless, the representativeness of these dissipation length scales is questionable as they depend on the interval over which the lengths are integrated. Two sets of characteristic lengths are presented. One corresponds to the external field (domain II) and the other to the interaction region. For the same flow condition, they provide quite different values. Furthermore, due to the intermittency of the boundary layer free-stream turbulence interface, it is difficult to say which length-scale is seen by the boundary layer. Table 1 summarizes the turbulent intensity $Tu$ for the three free-stream turbulent field cases $A$, $B$ and $C$.

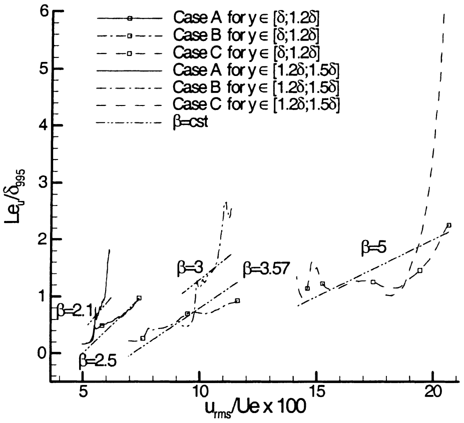

Fig. 5. Sample free-stream turbulent field dissipation length-scale and turbulent intensities.

Table 1

Turbulent intensity of the three free-stream turbulent fields presented

| Case of turbulence | Tu (%) at the interface of the domain I and II | Mean Tu (%) in the domain II |
|---|---|---|
| *A* | 7 | 6 |
| *B* | 12 | 11 |
| *C* | 21 | 21 |

## 4. Results

### 4.1. Influence of the free-stream turbulence on the turbulent boundary layer

The interpretation of the results is quite difficult if we restrict our analysis to what has been done in experiments. Indeed, as pointed out in Section 3.2, the turbulent field penetrates the boundary layer progressively. Examining Fig. 6, we can see that the influence of the free-stream turbulence is important at the entrance of the domain, where the Reynolds number $Re_x$ is equal to $4.6 \times 10^5$, and then progressively diminishes. The increase of $C_f$ at the entrance may be explained by the adaption of the flow to the new conditions in the outer zone.

The fact that for all free-stream turbulence intensities investigated here the increase in friction coefficient is about the same, is surprising. This is grist to mill for those who believe that free-stream turbulence does not influence the dynamic properties of the boundary layer. Fig. 7 shows that, except for a slight decrease in the logarithmic slope, the velocity profiles are similar to those observed experimentally. The wake vanishes while the viscous sublayer and logarithmic region are not influenced by free-stream turbulence. This is not the case for the temperature profile (see Fig. 8) for which the slope of the logarithmic region varies significantly with $Tu$. Fig. 9 shows that the evolution of the Stanton number follows the friction coefficient for $X \leqslant 6.2$ m. Considering the expression of the Stanton number $St = q''_{\mathrm{w}}/(\rho U_\infty c_{\mathrm{p}}(T_{\mathrm{w}} - T_\infty)) = (T^* u_\tau)/(U_\infty(T_{\mathrm{w}} - T_\infty))$, where $T^*$ is obtained from $T^+ = Pry^+$ and $T^+ = (T_{\mathrm{w}} - T)/T^*$, the drop is consistent with the behavior of a passive scalar subjected to the evolution of a velocity field. Indeed, we see that in this region the Stanton number increase, with respect to the case of no external turbulence, is the same for all $Tu$ values. Since the free-stream turbulent field enters

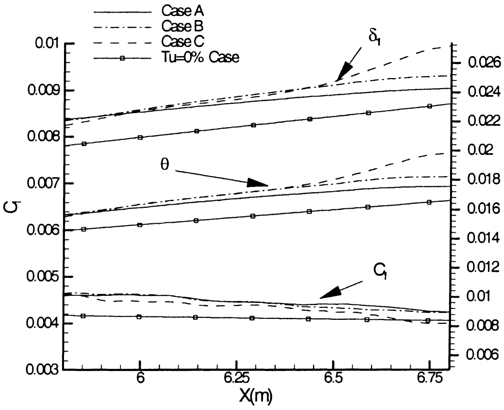

Fig. 6. Influence of the free-stream turbulence on the dynamic characteristic of the TBL.

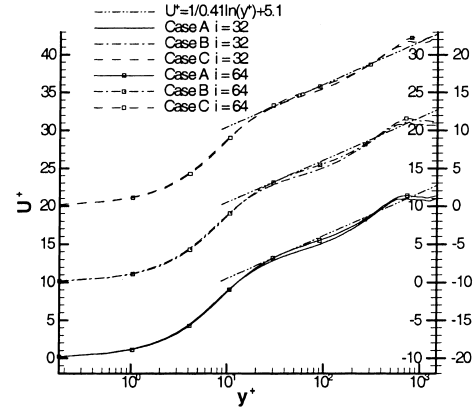

Fig. 7. Influence of the free-stream turbulence on the mean velocity profile.

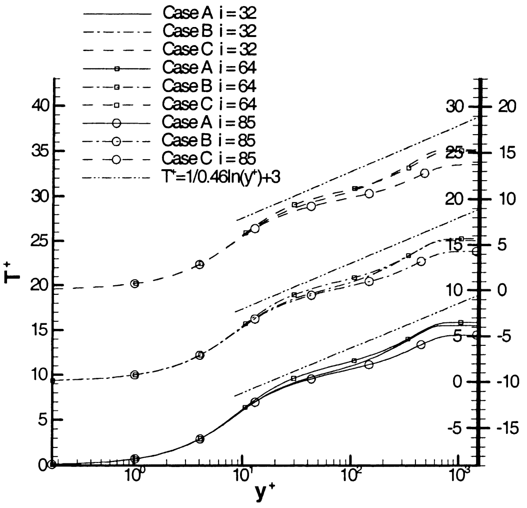

Fig. 8. Influence of the free-stream turbulence on the mean temperature profile.

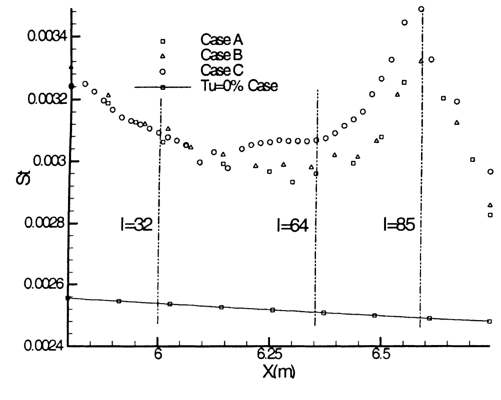

Fig. 9. Influence of the free-stream turbulence on heat transfter coefficient (vertical lines represent the number of the cells from the entrance of the domain in the streamwise direction).

the computational domain with a homogeneous temperature, we cannot expect a strong thermal interaction in the first cells of the domain as the thermal boundary layer does not have to merge with a turbulent thermal field.

One of the most interesting features in Fig. 9 is the rapid increase of the Stanton number for $6.2 \leqslant X \leqslant 6.65$ m, where a net influence of the free-stream turbulence intensity is observed, indicating a strong thermal interaction between the free-stream and the boundary layer.

As Fig. 4 shows, the turbulent intensity $Tu$ in the wake of the turbulent boundary layer increases with $x$. The different behavior of the thermal field can be attributed to a higher sensitivity to the level of turbulence in the wake. The various thicknesses presented in Fig. 10 are curve-fits using polynomials with a maximum deviation of 3%. When compared to the dynamic thickness presented in Fig. 6, we note that the temperature field is progressively influenced by the free-stream turbulent field starting at the entrance. Moreover, higher $Tu$ values yield a larger increase in the integral thickness, consistent with the observations of Dyban et al. (1977). A significant increase of the energy thickness

$$\delta_3 = \int_0^{\delta_T} (U/U_\infty)(1 - (U/U_\infty)^2)\, \mathrm{d}y$$

and of the thermal boundary thickness $\delta_T$ defined as the distance where $T = 0.005T_\mathrm{w}$ is observed, while at the same time the enthalpy thickness

$$\Delta = \int_0^{\delta_T} (U/U_\infty)((T - T_\infty)/(T_\infty - T_\mathrm{w}))\, \mathrm{d}y$$

is decreasing implying a flattening of the temperature profile.

The rapid fall of the Stanton number of $X \geqslant 6.65$ m is a numerical artifact due to the increase in the longitudinal mesh size, resulting in some numerical dissipation of the thermal and dynamic fluctuations.

In Fig. 11, we present the turbulent energy production profiles for the three different free-stream turbulent intensities. These profiles are compared to the result obtained with the same code for the case of $Tu_\infty = 0\%$. The increase in the production is not significant, despite the slight increase in the friction coefficient (≈10%), and the peak of production remains at about $y^+ = 12$.

The most important feature is the noticeable relative increase of the turbulent energy production in the logarithmic region and in the wake. The analogy with the $\langle u'v' \rangle$ profiles (see Fig. 12) indicates that the increase in turbulent energy production is due to a reorganization of the free-stream structures penetrating the boundary layer. Indeed, in the logarithmic and wake regions $\langle u'v' \rangle \gg \langle u'v' \rangle_\infty$, where $\langle u'v' \rangle_\infty$ is the mean value of the correlation $\langle u'v' \rangle$ in the free-stream turbulent field. We see also that the peak of $\langle u'v' \rangle$ not only increases with $Tu$, but is also displaced towards the wake. No modification of the viscous sublayer and buffer region is observed in Fig. 12. This may partly explain the weak increase in friction coefficient in

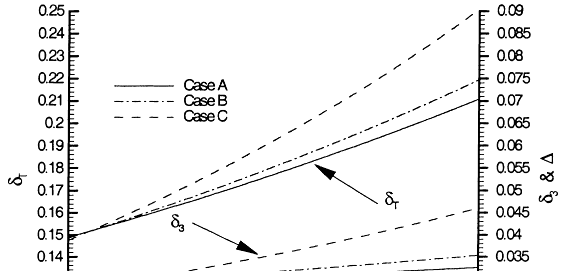

Fig. 10. Influence of the free-stream turbulence on the thermal characteristic of the TBL.

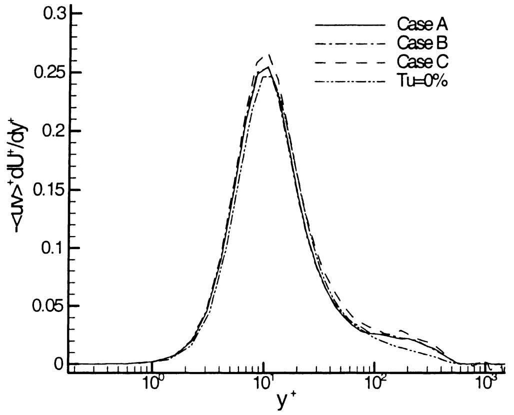

Fig. 11. Influence of the free-stream turbulence on the turbulent energy production profile at $i = 64$.

our simulation. Examination of Fig. 13 underlines that the increase of the kinetic energy linked to the reorganization of the structures when penetrating the boundary layer induces an important increase of the thermal fluctuations and hence of the Stanton number.

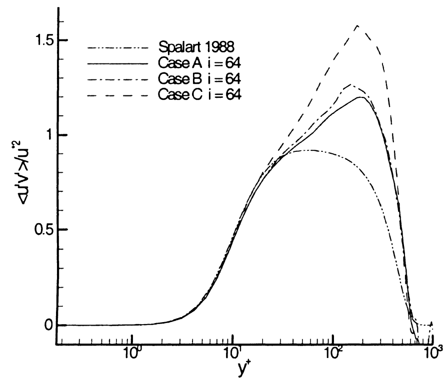

Fig. 12. Influence of the turbulent free-stream on the Reynolds stress $\langle u'v' \rangle$.

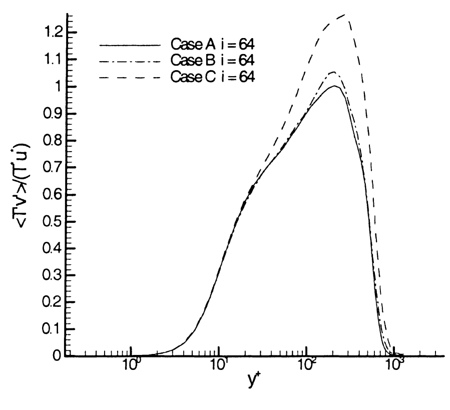

Fig. 13. Influence of the free-stream turbulence on the Reynolds stress $\langle T'v' \rangle$ at $i = 64$.

### 4.2. Influence of free-stream turbulence on the structure of the boundary layer near the leading edge

The problem linked to the progressive influence of the free-stream turbulent field on the dynamic and thermal boundary layer presented above did not allow us to faithfully reproduce the conditions under which experiments were conducted. To achieve this goal and examine if the history of the development of the boundary layer under a free-stream turbulent field has an influence on the heat and dynamic transfer, we undertook a simulation of the arrival of a highly turbulent field on the leading edge of a flat plate. Fig. 14 shows a schematic of the numerical simulation discussed in this section. It is the laminar region which is of interest in this section. LES of this flow was performed for case *B* and *C* of the turbulent fields presented earlier. The simulations are performed from the leading edge ($Re_x = 0$) to a Reynolds number of 38 000 in five successive spatial simulations performed on the domain of calculation in which the turbulent fields have been created (Péneau, 1999).

The analysis of the dynamic and thermal field near the leading edge of the flat plate shows streak-like structures appearing in the viscous region of the boundary layer. The energy of these structures increases with streamwise distance (Péneau, 1999) and accounts for production of turbulent energy as shown in Fig. 15. The amplitude of the peak of $\langle u'v' \rangle \partial U/\partial y$ is of the same order as in a fully turbulent boundary layer for a Reynolds number of 38 000, and underlines the fact that a kind of "bypass" transition occurs as a result of the high free-stream turbulence.

The formation of a wake region in the boundary layer in Fig. 16 confirms this bypass transition and is consistent with the observations of Dyban et al. (1977). The difference of slope

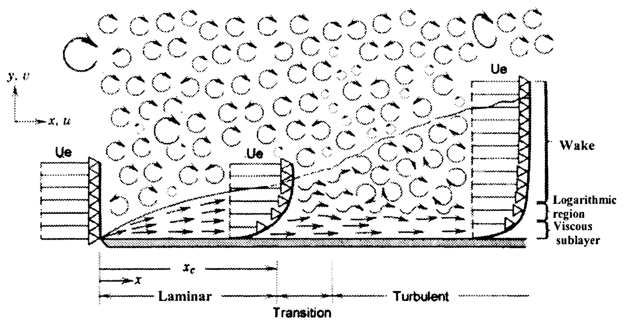

Fig. 14. Evolution of a boundary layer under the influence of a high free-stream turbulent field.

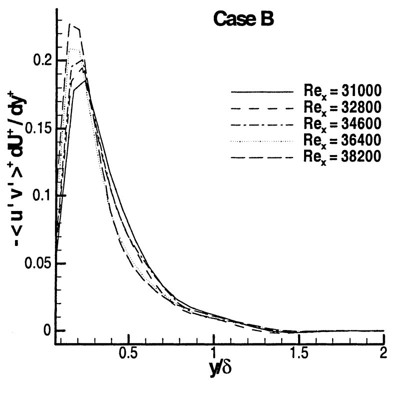

Fig. 15. Spatial evolution of the production of turbulent energy inside the boundary layer.

of the velocity profile shows the significant increase of the friction coefficient compared to the laminar value of the Blasius profile. Similar increases in wall transfer rates are also observed for the corresponding thermal field as shown in Fig. 17.

In Fig. 18, we see that at $Re_x = 31\,000$ the relative increase of friction coefficient and Stanton number is 100% and 70%, respectively, for a free-stream $u_{\mathrm{rms}} = 0.11$ m/s with $Tu = 9\%$. These figures highlight many important phenomena occurring between the free-stream turbulent field and the flat plate boundary layer during the initial phase of interaction, and the primary importance of the history of the development of the boundary layer under the free-stream field. This also helps to explain some of the contradictory experimental results reported in the literature which can be attributed to the different experimental conditions.

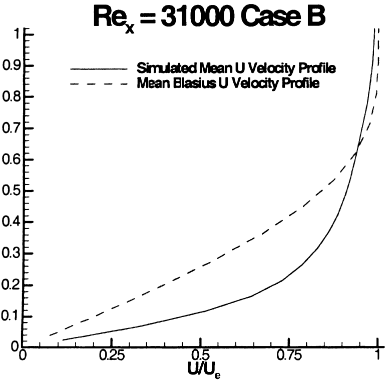

Fig. 16. $U$ velocity profile of a boundary layer.

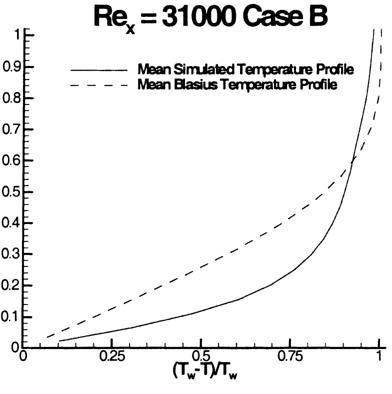

Fig. 17. Temperature profile of the boundary layer developed under a high free-stream turbulent field.

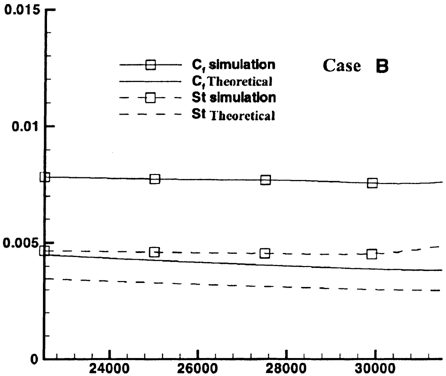

Fig. 18. Evolution of the friction coefficient $C_{\mathrm{f}}$ and Stanton number $St$.

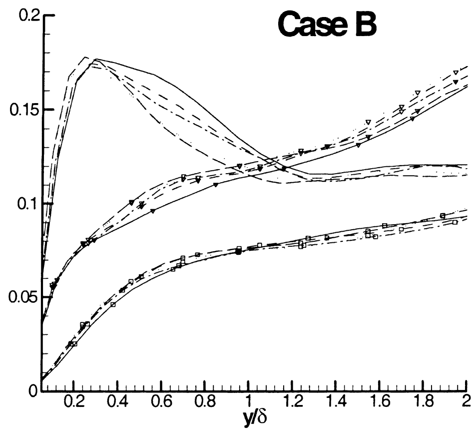

Fig. 19. Turbulent intensity profiles inside the boundary layer. No symbol (upper curve): $u_{\mathrm{rms}}$; $\nabla$: $w_{\mathrm{rms}}$; $\square$ (lower curve): $v_{\mathrm{rms}}$;—: $Re_x = 24\,000$; ---: $Re_x = 25\,800$; –·–: $Re_x = 27\,600$; ···: $Re_x = 29\,400$; –––: $Re_x = 31\,200$.

We now propose an interpretation of the interaction mechanism between the free-stream and the boundary layer. As shown in Table 1, the turbulent field $B$ has initially a mean turbulent intensity of $Tu = 11\%$. Examining Fig. 19, we see that the outside ($y \geqslant \delta$ the boundary layer thickness) turbulent intensity is 9%. The decrease with respect to the initial value is mainly due to the natural dissipation of energy with streamwise distance. What is more interesting in Fig. 19 is the peak of $u_{\mathrm{rms}}$ inside the boundary layer. This is higher than the maximum $u_{\mathrm{rms}}$ initially in the turbulent field $B$. The analysis of the turbulent intensity $v_{\mathrm{rms}}$ before and after the turbulent field $B$ had interacted with the flat plate shows that an important amount of the $v_{\mathrm{rms}}$ energy has been transferred to the $U$ velocity field in the first instants of the interaction. This transfer explains the $u_{\mathrm{rms}}$ profile of Fig. 19, and is due to the reorganization of the fluctuations of the free-stream turbulent field induced by the shear. The reorganization is at the origin of the appearance of streak-like structures. These structures then feed the production of turbulent energy, while maintaining the $u_{\mathrm{rms}}$ level in the boundary layer. For the temperature field, the importance of the Reynolds stress $\langle v'T' \rangle$ underlined in the previous simulation is confirmed. This stress is certainly the main vector by which turbulent energy enters the thermal boundary layer (Péneau, 1999). The difference of behavior between the dynamic and thermal field observed in the numerous experiments (Maciejewski and Moffat, 1992) is verified in these simulations with a faster thickening of the thermal boundary layer than the dynamic one. At $Re_x = 31\,000$, $\delta_T = 1.5\delta$, the wake region appears sooner in the thermal boundary layer and is larger than that for the dynamic boundary layer for the same Reynolds number. Further downstream, these features of the thermal field can be destabilizing and result in higher sensitivity to external perturbations.

## 5. Conclusions

Large eddy simulations of a spatially evolving boundary layer under high free-stream turbulence were undertaken using a dynamic mixed subgrid-scale model allowing integration to the wall. An effective method for generating free-stream turbulence and inlet boundary conditions were presented. Several factors make the analysis and interpretation of the results difficult. The problem in estimating the dissipation length scale perceived by the boundary layer was discussed. In agreement with experimentally observed trends, the simulations indicate a much greater sensitivity of the thermal field to free stream turbulence. The progressive penetration of the free-stream turbulence into the boundary layer may explain the relative insensitivity of the dynamic boundary layer to free-stream turbulent intensity. Whereas the velocity profiles remain essentially unperturbed, the temperature profiles exhibit a disppearance of the logarithmic region as well as a noticeable increase in the wake region with increasing free-stream turbulent intensity. This is accompanied, in the second half of the flow, by a rapid increase in the wall heat transfer coefficient as well as in the characteristic thicknesses of the thermal boundary layer. Based on an analysis of the various Reynolds stresses, it appears that the augmentation of the Stanton number correlates with $\langle v'T' \rangle$. To further investigate the influence of the development history of the boundary layer under a high free-stream turbulence field, new simulations were carried out in which the free-stream turbulent field attacks the flat plate from the leading edge. These simulations confirm the importance of the $\langle v'T' \rangle$ Reynolds stress in the interaction mechanisms between the constant temperature external turbulent field and the thermal boundary layer. The history of development of the dynamic boundary layer plays an important role in the increase of the dynamic transfer. A kind of "bypass" transition is observed giving rise to mechanisms of turbulent energy production.

## Acknowledgements

This work was part of a joint program INRA-CNRS. A BDI grant awarded to F. Péneau is gratefully acknowledged. We thank Dr. A. Kondjoyan for his fruitful contributions. We also thank our colleagues Dr. J. Magnaudet and Dr. D. Legendre for their contribution to the numerical part.

## References

Baskaran, V., Abdellatif, O.E., Bradshaw, P., 1989. Effects of free-stream turbulence on turbulent boundary layers with convective heat transfer. In: Proceedings of the Seventh Symposium on Turbulent Shear Flows, Standford University.

Blair, M.F., 1983. Influence of free-stream turbulence on turbulent boundary layer heat transfer and mean profile development, part II – analysis of results. J. Heat Transfer 105, 41–47.

Calmet, I., Magnaudet, J., 1996. Large eddy simulation of high-Schmidt number mass transfer in a turbulent channel flow. Phys. Fluids 9 (2), 438–455.

Dyban, E.P., Epik, E.Y., Surpun, T.T., 1977. Characteristic of the laminar layer with increased turbulence of the outer stream. Int. Chem. Engrg. 17 (8), 501–504.

Germano, M., Piomelli, U., Moin, P., Cabot, W.H., 1991. A dynamic subgrid-scale eddy viscosity model. Phys. Fluids A 3 (7), 1760–1765.

Hancock, P.E., Bradshaw, P., 1983. The effect of free-stream turbulence on turbulent boundary layer. J. Fluids Engrg. 105, 284–289.

Hancock, P.E., Bradshaw, P., 1989. Turbulence structure of a boundary layer beneath a turbulent free stream. J. Fluid Mech. 205, 45–76.

Maciejewski, P.K., Moffat, R.J., 1992. Heat treansfer with very high free-stream turbulence: Part II Analysis of results. ASME J. Heat Transfer 114, 834–839.

Magnaudet, J., Rivero, M., Fabre, J., 1995. Accelerated flows past a rigid sphere or a spherical bubble. Part I Steady straining flow. J. Fluid Mech. 284, 97–135.

Péneau, F., 1999. Etude numérique par simulation des grandes échelles de l'influence d'une forte turbulence extérieure sur les treansferts pariétaus au sein d'une couche limite. Ph.D. thesis, Institut Polutechnique de Toulouse.

Péneau, F., Legendre, D., Magnaudet, J., Boisson, H.C., 1999. Large eddy simulation of a spatially growing boundary layer using a dynamic mixed subgrid-scale model. In: Symposium ERCOFTAC on Direct and Large Eddy Simulation. Cambridge, May 1999.

Smagorinsky, J., 1963. General circulation experiments with the primitive equations. Mon. Weather Rev. 93, 99.

Zang, Y., Street, R.L., Koseff, J.R., 1993. A dynamic mixed subgrid-scale model and its application to turbulent recirculating flows. Phys. Fluids A 5 (12), 3186–3196.